Journal of Oceanography (2022) 78:495–513
https://doi.org/10.1007/s10872-022-00656-3

ORIGINAL ARTICLE

Identification of Kuroshio meanderings south of Japan via a topological data analysis for sea surface height

Takashi Sakajo[1,3] · Shun Ohishi[2,3,4] · Tomoki Uda[5]

Received: 14 January 2022 / Revised: 27 June 2022 / Accepted: 6 July 2022 / Published online: 31 July 2022

Abstract

This study proposes an algorithm to identify stable Kuroshio meanderings by extracting topological features from a sea surface height (SSH) gridded dataset in 1993–2020. Based on the mathematical theory of topological classifications for streamline patterns, the algorithm provides a unique symbolic representation and a discrete graph structure, which is referred to as the *partially cyclically ordered rooted tree (COT) representation* and the *Reeb graph*, respectively, to structurally stable Hamiltonian vector fields. We have confirmed that the temporal variations in the Kuroshio southernmost position south of the Tokai district captured by the algorithm are well consistent with the existing results by the Japan Meteorological Agency (JMA). The algorithm based on the topology detects five meandering periods: The three of them correspond to large meandering events detected by the JMA, while the two of them are offshore non-large meandering events. The topological data analysis reveals that a large cyclonic eddy inside of the meandering is split into two small eddies near the termination of the most meandering events.

Keywords Topological flow data analysis · Kuroshio, large meander · Offshore non-large meander · Hamiltonian vector field · Reeb graph · Sea surface height

1 Introduction

The Kuroshio is the western boundary current in the North Pacific subtropical gyre. It originates from the northern branch of the North Equatorial Current off the Philippines, flowing north-northeastward in the East China Sea. After it passes through the Tokara Strait south of the Kyushu, it turns to follow south of Japan, separates from the Boso Penisula, and finally flows into the Pacific basin as the Kuroshio Extension. As pointed out by Kawabe (1995), the Kuroshio path south of Japan undergoes interannual to decadal variations which might be classified into three typical types (Fig. 1a): the nearshore non-large meander (nNLM), offshore non-large meander (oNLM), and large meander (LM). The Kuroshio flows straight along the southern coast of Japan without meanderings during the nNLM period, whereas it meanders south of the Kanto and Tokai districts with a cool cyclonic eddy during the oNLM and LM periods, respectively. Thus, the Kuroshio has a southward meandering in both oNLM and LM periods but at different positions.

The Kuroshio path variations have substantial impacts on the fisheries such as sardine and anchovy catches (Nakata et al. 2000), marine transport, and Japanese weather such as hot summer (Sugimoto et al. 2020) and winter heavy snowfall (Nakamura et al. 2012) in the Kanto district during the LM period. Consequently, ocean predictions with a focus on the Kuroshio path have been conducted using high-resolution regional ocean data assimilation systems (e.g. Miyazawa et al. 2005; Usui et al. 2006; Hirose et al. 2019), and the information has been provided to users such as fisheries and marine transport companies. (Miyazawa et al. 2009; http://www.jamstec.go.jp/jcope/htdocs/e/kow/index.html).

✉ Takashi Sakajo
sakajo@math.kyoto-u.ac.jp

[1] Department of Mathematics, Kyoto University, Kitashirakawa Oiwake-cho, Sakyo-ku, Kyoto 606-8502, Japan

[2] RIKEN Center for Computational Science, Kobe, Japan

[3] RIKEN Cluster for Pioneering Research, Kobe, Japan

[4] Institute for Space-Earth Environmental Research, Nagoya University, Nagoya, Japan

[5] Advanced Institute for Materials Research (WPI-AIMR), Tohoku University, Sendai, Japan

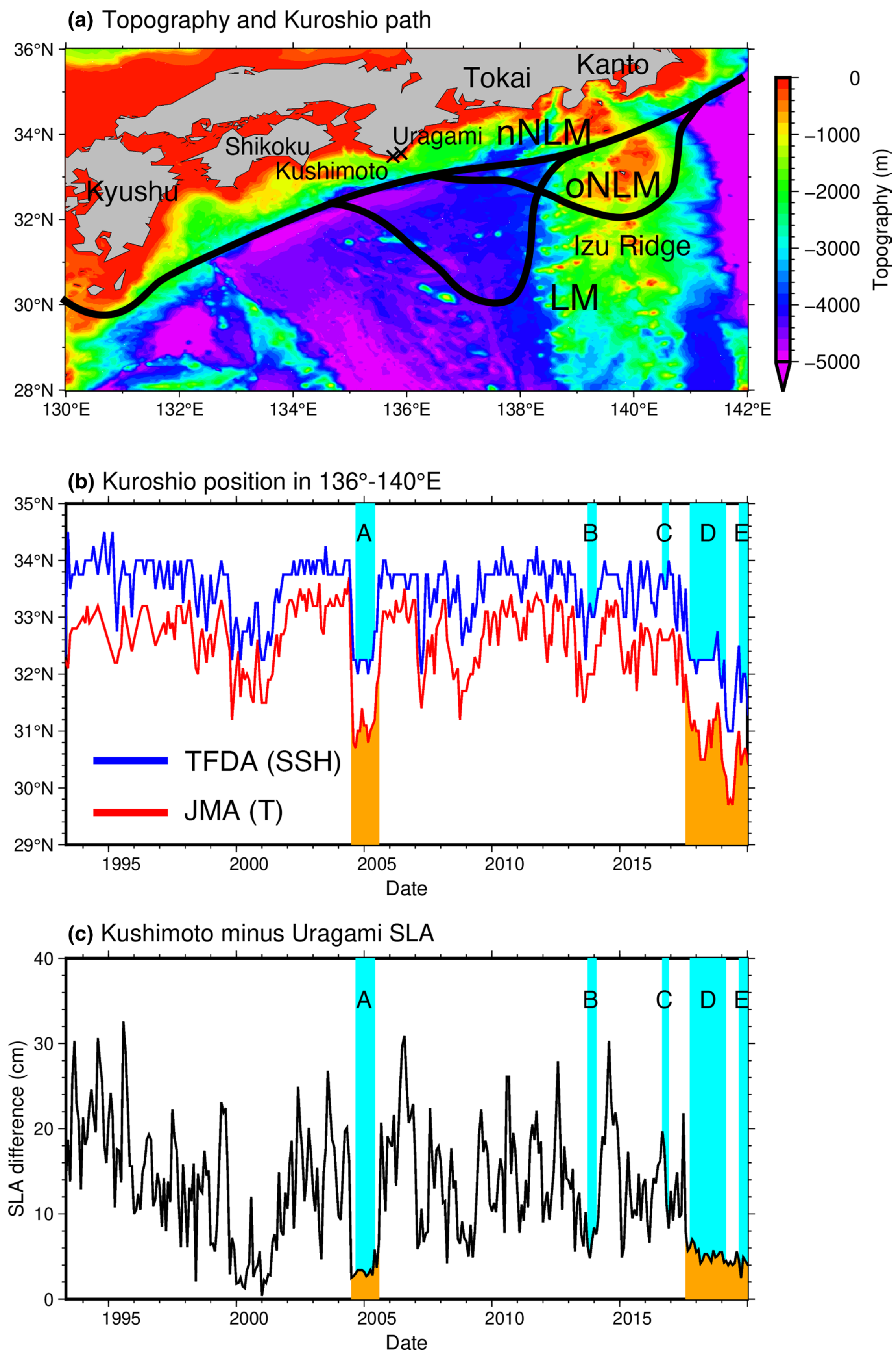
(a) Topography and Kuroshio path
36°N
34°N
32°N
30°N
28°N
130°E
132°E
134°E
136°E
138°E
140°E
142°E
Tokai
Kanto
Shikoku
Uragami
nNLM
Kushimoto
Kyushu
oNLM
Izu Ridge
LM
0
−1000
−2000
−3000
−4000
−5000
Topography (m)
(b) Kuroshio position in 136°-140°E
35°N
34°N
33°N
32°N
31°N
30°N
29°N
A
B
C
D
E
TFDA (SSH)
JMA (T)
1995
2000
2005
2010
2015
Date
(c) Kushimoto minus Uragami SLA
40
30
20
10
0
SLA difference (cm)
A
B
C
D
E
1995
2000
2005
2010
2015
Date

◂**Fig. 1** **a** Topography (color) and three typical Kuroshio paths (black lines; Kawabe 1995): nearshore non-large meander (nNLM), offshore non-large meander (oNLM), and large meander (LM). **b** Southernmost latitude of the Kuroshio path in 136°–140°E off the Tokai district estimated by the Japan Meteorological Agency (JMA; red) and *topological flow data analysis* (TFDA; blue). **c** Sea level anomaly difference between Kushimoto and Uragami from the JMA. In **a**, the locations of Kushimoto, Uragami, Tokai and Kanto districts, Izu Ridge, and Shikoku and Kyushu Islands are shown. In **b** and **c**, orange (cyan) color indicates the LM (meandering) periods detected by the JMA (the TFDA algorithm developed in this study), and capital letters A–E denote the meandering periods detected by the TFDA algorithm

To detect the LM events, the Japan Meteorological Agency (JMA) constructs a time series of the southernmost latitude of the Kuroshio path in 136°–140°E south of the Tokai district using temperatures at 200 m depth and satellite sea surface temperatures (SSTs) (Fig. 1b). The sea-level differences between Kushimoto and Uragami from historical tide gauge measurements are also used as an indicator, because the difference tends to be small during the LM periods (Fig. 1c) (Kawabe 1980). In addition, specific sea surface height (SSH) contour and maximum flow speed at the sea surface and 100 m depth are assumed to be the Kuroshio axis in the previous studies (Ambe et al. 2004; Miyazawa et al. 2005; Usui et al. 2006, 2013; Tsujino et al. 2006; Aoki et al. 2020). However, since the abundant fronts and eddies result in complex flow fields such as bifurcated strong currents around the Kuroshio region (figure not shown), these existing methods might not accurately capture the spatiotemporal variations in the Kuroshio path. Therefore, an objective algorithm is required to classify the Kuroshio path.

Since orbital satellites have been observing SSH anomalies and the accurate mean dynamic ocean topography is derived from surface drifter buoys and atmospheric datasets (Maximenko et al. 2009), observation-based SSH datasets with sufficient skill in reproducing the geostrophic flow field are available since late 1992 (Ducet et al. 2000; Taburet et al. 2019). For the SSH $h(x, y)$ on $(x, y) \in D \subset \mathbb{R}^2$, the geostrophic flow $\boldsymbol{u}_g$ is defined by $f\boldsymbol{k} \times \boldsymbol{u}_g = -g\nabla h$ [i.e. $\boldsymbol{u}_g = -g/f(\partial h/\partial y, -\partial h/\partial x)$], where f is the vertical component of the Coriolis parameter, $\boldsymbol{k}$ is the unit vector in the vertical direction and $g(= 9.8ms^{-2})$ is the gravitational acceleration. Since the velocity field $\boldsymbol{u}$ is approximately represented by $\boldsymbol{u} = \boldsymbol{u}_g + \boldsymbol{u}_a \approx \boldsymbol{u}_g$ around western boundary current regions where the geostrophic flow is much stronger than the ageostrophic flow $\boldsymbol{u}_a$ (i.e., $\boldsymbol{u}_g \gg \boldsymbol{u}_a$). Moreover, owing to $\nabla h \bullet \boldsymbol{u}_g = 0$, the contour lines of the SSH h are equivalent to streamlines characterizing geometric features of the Kuroshio current. Since the Kuroshio path entraps a cyclonic eddy off the Tokai–Kanto districts south of Japan in the meandering periods, it would be possible to detect meandering occurrence and termination by extracting the eddy flow structure in terms of topology from a gridded SSH dataset.

Yokoyama and Sakajo (2013) have developed a mathematical theory classifying the topological structure of streamlines of Hamiltonian vector fields in a uniform flow. In this theory, the vector fields are assumed to be *structurally stable*. By structural stability, we mean that the topological structure of streamlines is unchanged under small perturbations in the space of continuously differentiable functions. Based on the theory, the previous studies (Yokoyama and Sakajo 2013; Sakajo and Yokoyama 2018; Uda et al. 2019) demonstrated that the topological structure of streamlines generated by structurally stable Hamiltonian vector fields is in one-to-one correspondence with discrete graph structure, called *Reeb graphs*, and their associated symbolic expressions, called *partially cyclically ordered rooted tree (COT) representations*. *Topological flow data analysis (TFDA)* is a new method of data analysis using the unique Reeb graph and its associated COT symbol expressing the topological structure of particle orbits generated by two-dimensional vector fields. We note that the assumption of structural stability does not give rise to critical restriction theoretically or practically. Since structurally unstable Hamiltonian vector fields immediately transfer to structurally stable ones subject to infinitely small perturbations, they are approximated by a sequence of structurally stable Hamiltonian vector fields. Moreover, in practical data analyses, since data usually contain noise and errors, structurally unstable flows hardly appear. Based on the topological classification theory for structurally stable Hamiltonian vector fields, this study aims to characterize the Kuroshio meandering states in terms of topology, thereby detecting the occurrence and termination of the meanderings from the observational SSH dataset. Datasets used in this study are introduced in Section 2. In Section 3, after reviewing the topological classification theory for structurally stable Hamiltonian vector fields, we show some snapshots that TFDA applied to the SSH dataset. We also introduce the algorithm detecting the meandering periods. In Section 4, applying the algorithm to the SSH dataset from January 1993 to April 2020, we show detected meandering periods and validate the results by TFDA with those by JMA. Furthermore, we discuss the relationship between temporal changes in entrapped eddy structure and the Kuroshio path. The summary is given in the last section.

2 Data

In this study, we use a gridded SSH dataset from Archiving, Validation and Interpretation of Satellite Oceanographic data (AVISO; Ducet et al. 2000; Taburet et al. 2019) with horizontal resolution of 0.25° from January 1993 to April 2020. We adopt the monthly Kuroshio southernmost latitude in 136°–140°E (https://www.data.jma.go.jp/kaiyou/data/shindan/b_2/uroshio_stream/kuro_slat.txt) from the JMA, which is estimated by SSTs, temperatures at 200 m depth, and the monthly sea level differences from tide gauge measurements between Kushimoto and Uragami (https://www.data.jma.go.jp/kaiyou/data/shindan/b_2/uroshio_stream/ksur.txt). Here, the JMA datasets are utilized not to compare the ability with TFDA, but to validate results by our TFDA method. We also use the Kuroshio transport across the 137°E section in summer and winter (https://www.data.jma.go.jp/gmd/kaiyou/data/shindan/b_2/uroshio_flow/kt137.txt) provided by the JMA. We note that the Kuroshio southernmost latitude dataset contains about 35% missing values in 1993–99.

3 Topological flow data analysis (TFDA) for detecting Kuroshio meanderings

3.1 Topological classification theory of streamline patterns

When a two-dimensional vector field $\boldsymbol{u}(x,y) = (u(x,y), v(x,y))$ on a domain $(x,y) \in D \subset \mathbb{R}^2$ is incompressible, i.e. divergence free, there exists a scalar function called the Hamiltonian or stream function $H(x,y)$. The vector field is given by $u = \partial H/\partial y$ and $v = -\partial H/\partial x$, and it is called the Hamiltonian vector field. As clear from $\nabla H \bullet \boldsymbol{u} = 0$, particle orbits in the Hamiltonian vector field are identical to contour lines of the Hamiltonian H referred to as streamlines. As discussed in Sect. 1, the geostrophic vector field can be regarded as a structurally stable Hamiltonian vector field in a uniform flow, where the Hamiltonian is equivalent to the SSH.

Figure 2 shows all topological streamline patterns appearing in structurally stable Hamiltonian flows in the uniform flow. A unique symbolic expression referred to as *a COT symbol* is assigned to each streamline pattern. The topological streamline patterns in Fig. 2a, b, d, g have been shown in Uda et al. (2021) in which atmospheric blocking events are detected via TFDA. Additionally, we present streamline patterns in Fig. 2c, e, f related to topographic boundaries (islands).

Figure 2a indicates a uniform flow referred to as *root structure*, whose COT symbol is represented by $a_\emptyset(\square_a^1 \cdot \cdots \cdot \square_a^n)$. Here, each box symbol $\square_a^i$ for $i = 1, \ldots, n$ in the COT symbol expresses that either a streamline pattern $a_\pm$ in Fig. 2b or a_2 in Fig. 2c is embedded in the uniform flow, i.e. $\square_a^i \in \{a_\pm, a_2\}$ for $i = 1, \ldots, n$. The COT symbols corresponding to these streamline patterns are arranged in order by picking them up from bottom to top when the uniform flow direction is from left to right.

Figure 2b shows streamline patterns with a self-connected saddle separatrix embedded in the root structure. To distinguish the flow directions of the saddle separatrix, we assign the COT symbol $a_+(\square_{b_+})$ $[a_-(\square_{b_-})]$ to the streamline pattern when the flow along the saddle separatrix turns in the counter-clockwise (clockwise) direction. The streamline pattern inside the self-connected saddle separatrix is chosen from either $b_{\pm\pm}$, $b_{\pm\mp}$ in Fig. 2d, $\beta_\pm$ in Fig. 2f, or $\sigma_\pm$ in Fig. 2g, i.e. $\square_{b_\pm} \in \{b_{\pm\pm}, b_{\pm\mp}, \beta_\pm, \sigma_\pm\}$, in which double signs correspond.

As shown in Fig. 2c, a streamline pattern embedded in the root structure is represented by the COT symbol $a_2\left(\square_{c+s}, \square_{c-s}\right)$. This consists of a physical boundary with two saddles to which streamlines of the uniform flow are connected. Although this illustration schematically draws the boundary as a circular disc, it can be transformed continuously to any shapes, because the shape of the boundary does not affect TFDA results in terms of topology. Any number of streamline patterns c_- (c_+) are attached to the upper (lower) side of the boundary, and their details are described later. The box symbol $\square_{c\pm s}$ is an abbreviation for a sequence of streamline patterns of $c_\pm$, i.e. $\square_{c+s} = \square_{c_+}^1, \cdots, \square_{c_+}^s$ and $\square_{c-s} = \square_{c_-}^1, \cdots, \square_{c_-}^s$, respectively, where $s (> 0)$ is the number of the streamline patterns attached to the boundary.

Streamline patterns consisting of two self-connected saddle separatrices are shown in Fig. 2d. When the counter-clockwise (clockwise) saddle separatrices form a figure eight pattern, the COT symbol $b_{++}\{\square_{b_+}, \square_{b_+}\}$ $[b_{--}\{\square_{b_-}, \square_{b_-}\}]$ is assigned, where $\square_{b\pm}$ represents inner streamline patterns enclosed by the two saddle separatrices, and the parentheses $\{\bullet\}$ expresses that the inner streamline patterns are arranged in cyclic order. When one counter-clockwise (clockwise) saddle separatrix encloses the other clockwise (counter-clockwise) saddle separatrix, the COT symbol of the streamline pattern is given by $b_{+-}(\square_{b_+}, \square_{b_-})$ $[b_{-+}(\square_{b_-}, \square_{b_+})]$. The streamline patterns in $\square_{b\pm}$ are chosen from either a pattern of $b_{\pm\pm}$, $b_{\pm\mp}$, $\beta_\pm$, or $\sigma_\pm$.

An orbit connecting two saddles at the same boundary forms a streamline pattern denoted by the COT symbol $c_\pm$ (Fig. 2e). Inside the domain enclosed by the saddle separatrix and the boundary, it is necessary to embed one streamline pattern represented by $\square_{b_\pm} \in \{b_{\pm\pm}, b_{\pm\mp}, \beta_\pm, \sigma_\pm\}$. When the flow direction of the outer saddle separatrix is counter-clockwise (clockwise), the COT symbol $c_+\left(\square_{b_+}, \square_{c-s}\right)$

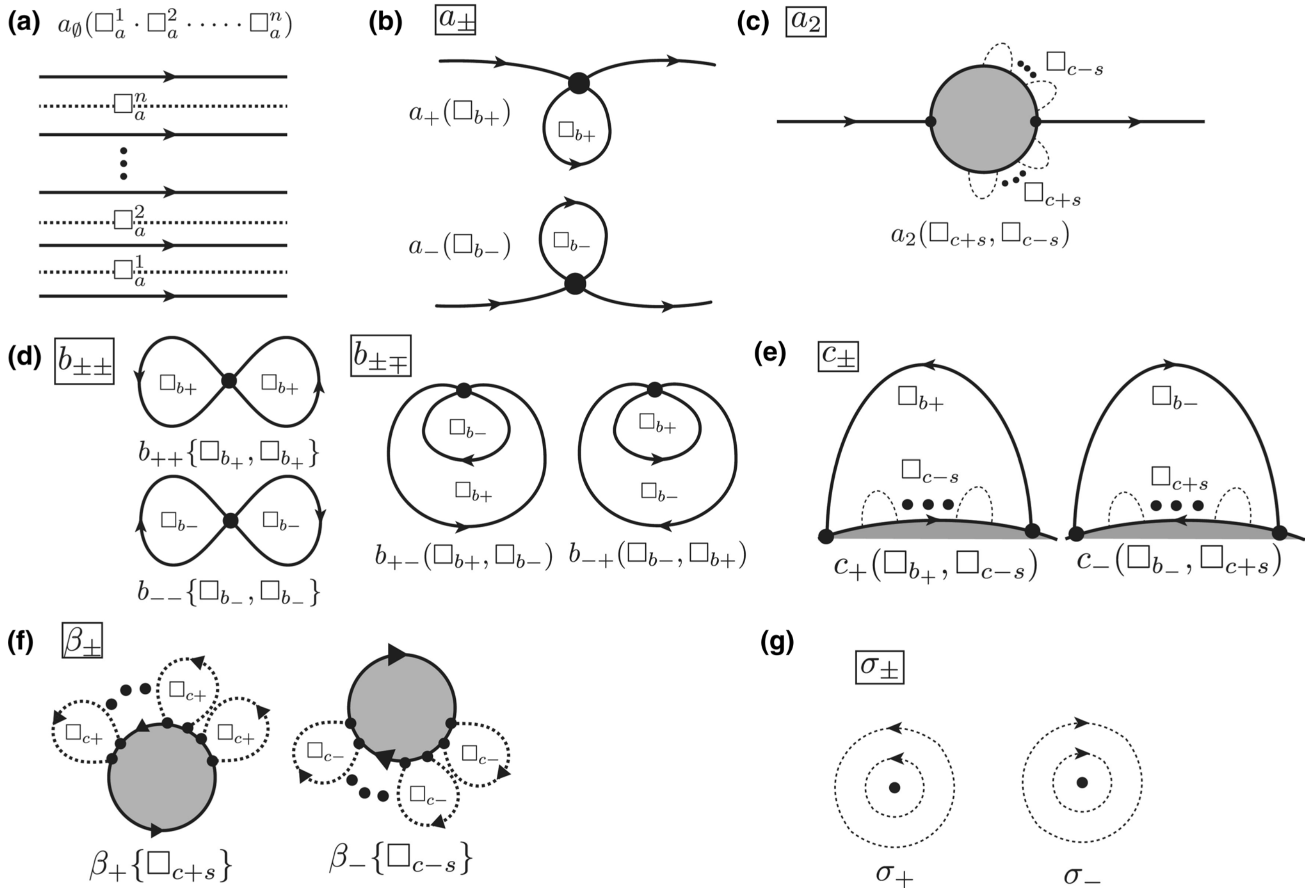

Fig. 2 *Partially cyclically ordered rooted tree (COT) symbols;* and their streamline patterns identified by TFDA. **a** A COT symbol $a_\emptyset(\square_a^1, \square_a^2, \cdots, \square_a^n)$; A uniform flow referred to as *root structure*. **b** $a_+(\square_{b_+})$ ($a_-(\square_{b_-})$); A streamline pattern with one self-connected saddle separatrix rotating counter-clockwise (clockwise). **c** $a_2(\square_{c+s}, \square_{c-s})$; A streamline pattern with a physical boundary having two saddles embedded in a uniform flow. **d** $b_{++}\{\square_{b+}, \square_{b+}\}$ ($b_{--}\{\square_{b-}, \square_{b-}\}$) in the left panel; A figure-eight streamline pattern with two self-connected saddle separatrices turning counter-clockwise (clockwise). $b_{+-}(\square_{b+}, \square_{b-})$ ($b_{-+}(\square_{b-}, \square_{b+})$) in the right panel; A streamline pattern with two self-connected saddle separatrices, where the inner clockwise (counter-clockwise) separatrix is enclosed by the outer counter-clockwise (clockwise) separatrix. **e** $c_\pm(\square_{b_\pm}, \square_{c\mp s})$; A saddle separatrix connecting two different saddles on a physical boundary. **f** $\beta_\pm\{\square_{c\mp s}\}$ ($\beta_\pm$) attached with (without) streamline structure $c_\pm$; An isolated physical boundary. **g** σ_+ (σ_-); An elliptic center surrounded by counter-clockwise (clockwise) periodic orbits in its neighborhood. We note that elliptic centers $\sigma_\pm$ and physical boundaries $\beta_\pm$ are innermost streamline patterns with no internal structure

$[c_-(\square_{b_-}, \square_{c+s})]$ is assigned. Here, any number of $c_\pm$ streamline patterns can be attached to the boundary, and the COT symbol $\square_{c_\pm}^{\mathrm{i}} \in \{c_+(\square_{b_+}, \square_{c-s}), c_-(\square_{b_-}, \square_{c+s})\}$ is arranged along the boundary in the flow direction.

An isolated physical boundary, to which any number of $c_\pm$ streamline patterns are attached, is shown in Fig. 2f. Its COT symbol is represented by $\beta_\pm\{\square_{c\pm s}\}$ with $\square_{c\pm s} = \square_{c_\pm}^1, \cdots, \square_{c_\pm}^{\mathrm{s}}$, in which the sign corresponds to the flow direction along the boundary, and $c_\pm$ streamline patterns are arranged in cyclic order. When any $c_\pm$ structure is not attached to the boundary, the COT symbol is simply denoted as $\beta_\pm$, and this is an innermost streamline pattern having no internal structure. Another innermost streamline pattern in structurally stable Hamiltonian flows is an isolated elliptic center associated with counter-clockwise (clockwise) periodic orbits in its neighborhood. Its COT symbol is denoted by σ_+ (σ_-) (Fig. 2g).

The procedure providing a unique COT representation for a given structurally stable Hamiltonian flow in the uniform flow is as follows. [See Uda et al. (2019) for the detailed description of the algorithm]: First, streamline patterns $a_\pm$ and a_2 are detected in the uniform flow, and then the COT symbols are arranged in the root structure $a_\emptyset(\square_a^1 \cdots \square_a^n)$, where $\square_a^{\mathrm{i}} \in \{a_\pm(\square_{b_\pm}), a_2(\square_{c+s}, \square_{c-s})\}$ for $i = 1, \dots, n$. Identifying inner streamline patterns of $b_{\pm\pm}$, $b_{\pm\mp}$, $\beta_\pm$, or $\sigma_\pm$ in the streamline patterns $a_\pm$ and a_2, the COT symbols are substituted in $\square_{b_\pm}$ and $\square_{c\pm s}$. Here, $\square_{b_\pm} \in \{b_{\pm\pm}\{\square_{b_\pm}, \square_{b_\pm}\}, b_{\pm\mp}\{\square_{b_\pm}, \square_{b_\pm}\}, \beta_\pm\{\square_{c\pm s}\}, \sigma_\pm\}$, and $\square_{c_\pm}$ is chosen from $c_\pm(\square_{b_\pm}, \square_{c\pm s})$. Repeating this step recursively to every streamline pattern until the streamline patterns reach innermost structure such as elliptic centers $\sigma_\pm$ and physical boundaries $\beta_\pm$, the COT representation for the structurally stable Hamiltonian flow is finally obtained. Furthermore, at every step in this procedure, by regarding the outer and embedded inner streamline patterns as parent and child nodes, respectively, the edges between these nodes are created. At the same time, the value of the Hamiltonian is associated with each node. This produces a planar acyclic graph with height values, called *Reeb graph*. As described in Sect. 1, it is mathematically assured that every structurally stable Hamiltonian vector field has a unique Reeb graph and its associated COT representation, and therefore they are utilized as topological identifiers of the Hamiltonian flow in terms of topology.

We have developed a practical software, *psiclone*, to compute the Reeb graph and its associated COT representation and perform TFDA for a given Hamiltonian gridded dataset. The software has the following two important functions useful for data analyses: First, defining the length of an edge as the height difference between nodes connected by the edge, edges with a shorter length than a prescribed threshold can be cut off. This function acts as a low-pass filter removing small-scale topological streamline patterns such as noises. Second, regions enclosed by saddle separatrices of streamline patterns $a_\pm$, $b_{\pm\pm}$, $b_{\pm\mp}$, and $c_\pm$ can be extracted, and they are referred to as *regions of influence*. This function plays an important role in detecting the Kuroshio meanderings from the SSH dataset.

3.2 Application of TFDA to the SSH dataset

Since the SSH contour lines correspond to geostrophic streamlines except for the tropical regions, we apply TFDA to the SSH dataset using *psiclone* to represent topological features of the geostrophic flows in the mid-latitude regions. While the slip boundary condition is assumed in the topological classification theory (Yokoyama and Sakajo 2013), this condition is not necessarily satisfied with the SSH dataset used in this study. In some cases, the no-slip boundary condition is adopted, but in other cases, the slip boundary condition is assumed. Hence, we have applied both slip and no-slip boundary conditions to TFDA. The original SSH dataset can be regarded to satisfy the slip boundary condition. On the other hand, to satisfy the no-slip condition, we adjust land grid cells along coastlines as follows: An SSH value at each land grid cell is set to that at an ocean grid cell normal to the land. As a result, we have confirmed that the results are the same regardless of the slip and no-slip boundary conditions. This is because any artificial saddles along the coastlines are not created by this procedure for the no-slip boundary condition.

In this study, to reduce computational costs, we restrict the analysis domain to off the southern-eastern coast of Japan as shown in Fig. 3. This is referred to as the *region of interest (ROI)* and denoted by Ω. We set the threshold of the length of an edge for the low-pass filter to be 4.0×10^{-2} m. As a result, small-scale structure, such that the SSH differences at both ends between nodes are smaller than the threshold, is not identified. We have confirmed that the qualitatively same results are obtained even if the different analysis domains and thresholds are applied.

Figure 3b shows an output of *psiclone* for the SSH dataset in December 2004 when the Kuroshio LM occurs south of the Tokai district (135°–140°E, 30°–35°N). The COT representation of this streamline pattern is described as

$$
\begin{aligned}
&a_\varnothing\big(a_-^0 \bullet a_+^1 \bullet a_+^2 \bullet a_-^3 \bullet a_-^4 \bullet a_2\big(c_+^0, \lambda\big) \\
&\quad \bullet a_-^6 \bullet a_-^7 \bullet a_-^8 \bullet a_+^9 \bullet a_+^{10}\big(b_{++}\big) \bullet a_+^{11}\big),
\end{aligned}
\tag{1}
$$

where λ denotes the non-existence of the streamline pattern for $\square_{c-s}$ in a_2. Here, the symbols $\sigma_\pm$ representing elliptic centers are not shown to reduce the length of the COT representation. The superscript numbers are assigned to the COT symbols $a_\pm$ and c_+ in (1) to identify which streamline patterns are represented by the COT symbols. A Reeb graph associated with the COT representation is also shown in the same panel. Nodes of the Reeb graph (red stars in Fig. 3b) are placed at saddle points for $a_\pm$ and b_{++} structure, elliptic centers, and a boundary saddle for the a_2 structure. Edges are drawn as gray segments connecting these nodes.

Here, we describe an important note about outputs from *psiclone*, which is caused by the opposite sign between the geostrophic and Hamiltonian velocity fields in the Northern Hemisphere with the positive Coriolis parameter ($f > 0$). As described in Sect. 1, the geostrophic velocity field is calculated from the SSH $h(x, y)$ through the formula $\boldsymbol{u_g} = g/f(-\partial h/\partial y, \partial h/\partial x)$, whereas *psiclone* assumes that the Hamiltonian vector field with a Hamiltonian H is given by $\boldsymbol{u} = (\partial H/\partial y, -\partial H/\partial x)$. This leads that the uniform flow direction in *psiclone* (Fig. 2a) is recognized as the opposite to the actual geostrophic flow. Consequently, in the *psiclone* calculation, the COT symbols $\square_a^i$ for $i = 1, \dots, n$ in $a_\varnothing$ are arranged from the left to the right by picking up $a_\pm$ and a_2 streamline patterns from the north to the south, and for instance the COT symbol a_+ (a_-) expresses an anticyclonic (cyclonic) eddy in the Northern Hemisphere.

Based on the COT representation (1) and its associated Reeb graph, the topological structure around the Kuroshio region is characterized (Fig. 3b). The sub-sequence $a_-^0 \bullet a_+^1 \bullet a_+^2$ in the COT representation correspond to the

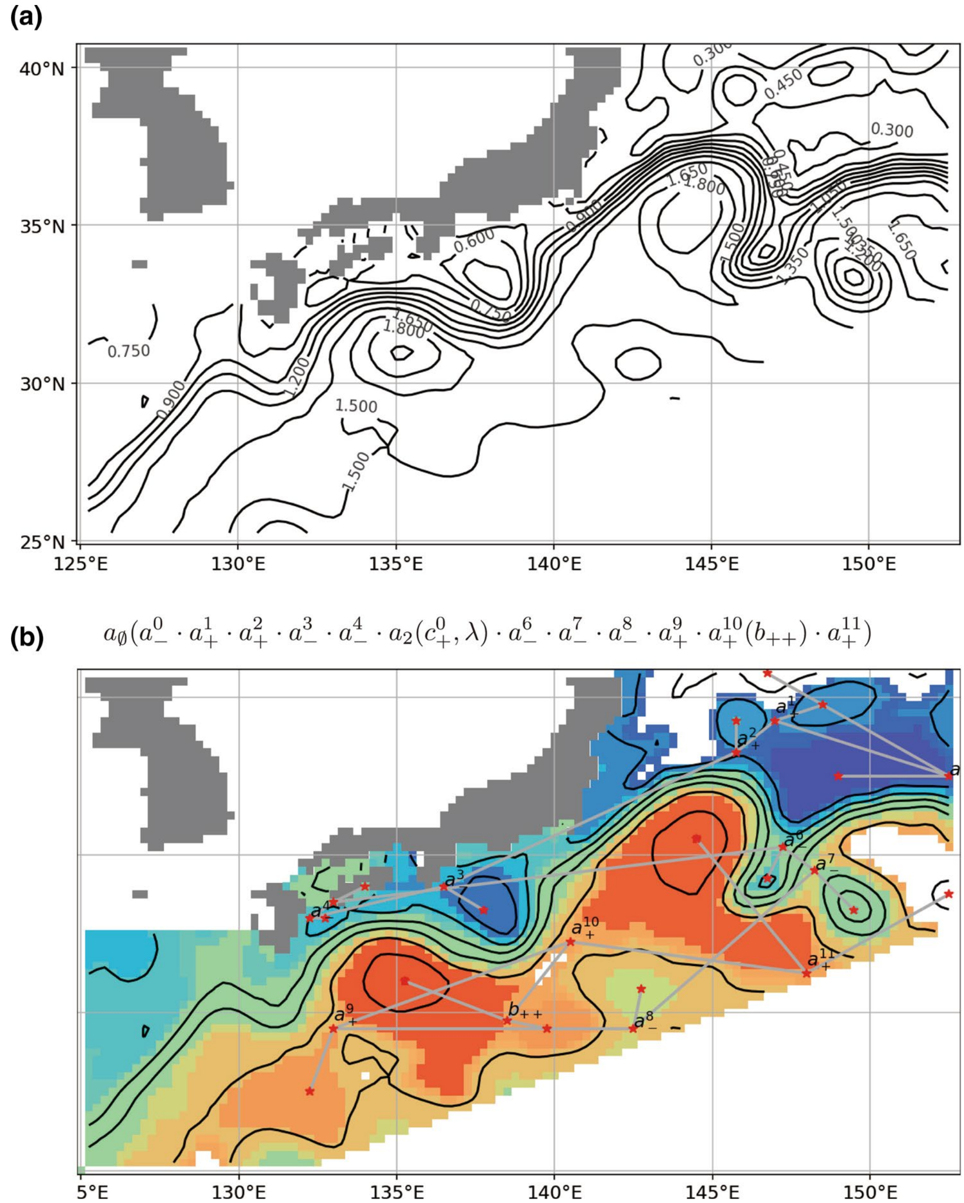

Fig. 3 **a** Monthly mean sea surface height (SSH) in the *region of interest* Ω in December 2004 when the Kuroshio LM occurs. **b** The COT representation of the streamline pattern at the header, nodes (red stars) and edges (gray segments) of the Reeb graph, and the partition plot associated with the COT representation (color). In **a**, the area with the contours indicates the region of interest. Contour intervals are 0.15 m

streamline patterns on the northern side of the Kuroshio Extension. Streamline patterns on the southern side of the Kuroshio and Kuroshio Extension are represented by the sub-sequence $a_-^6 \cdots a_+^{11}$ after a_2. The streamline pattern represented by a_-^3 has a self-connected saddle separatrix enclosing a cyclonic eddy associated with the LM between the Kuroshio and the southern coast of the Tokai district. The streamline pattern represented by a_-^4 is located between the Kyushu and Shikoku Islands on the northern side of the Kuroshio, and the COT symbol $a_2\left(c_+^0, \lambda\right)$ indicates that the Shikoku Island is a physical boundary with two boundary saddles connecting to the Kuroshio, entrapping an anticyclonic eddy represented by the COT symbol c_+^0.

In Fig. 3b, different colors are painted to show the flow domains surrounded by saddle separatrices of the streamline patterns $a_\pm$, b_{++}, c_+ (i.e. the regions of influence), and this color map is referred to as a *partition plot* associated with the COT representation. Each eddy is shaded by the different color, and therefore *psiclone* successfully extracts the regions of influence. The region of influence enclosed by the saddle separatrix of the streamline pattern a_-^3 south of the Tokai district (dark blue in Fig. 3b) indicates an area where the cyclonic eddy is entrapped by the Kuroshio during the LM period. Accordingly, area and geometric centers of the cyclonic eddies south off the Tokai and Kanto districts estimated from the region of influence enable us to detect the Kuroshio meanderings using TFDA.

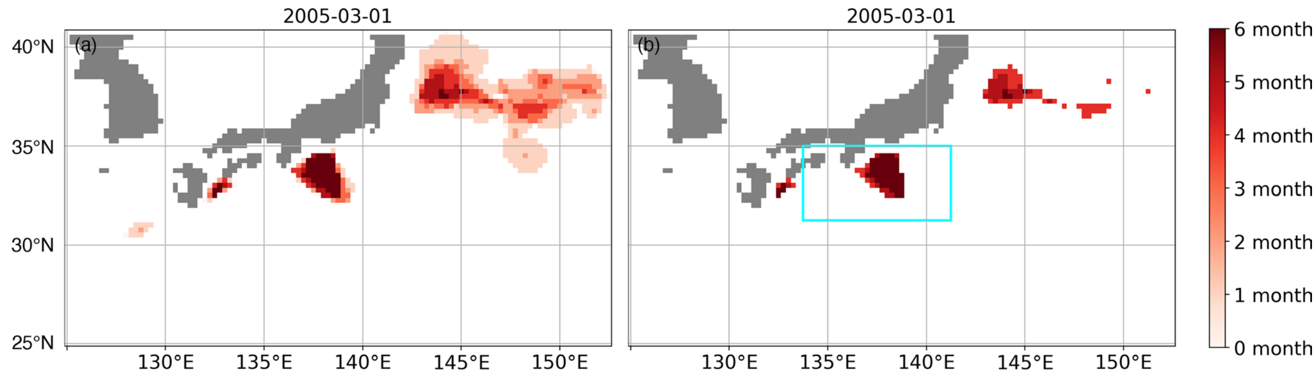

Fig. 4 **a** (left) Histogram $C_{t,\Delta t}(\boldsymbol{x})$ on $\boldsymbol{x} \in \Omega$ calculated from the SSH dataset in March 2005 using the 6-month analysis window. **b** (right) Connected components belonging to B_t, where $C_{t,\Delta t}(\boldsymbol{x})$ is larger than the threshold of 3 months

3.3 Algorithm detecting the Kuroshio meanderings

We develop a TFDA algorithm proposed for the detection of atmospheric blocking (Uda et al. 2021) to detect periods when the Kuroshio stably meanders southward south of Japan. The monthly mean SSH on $(x, y) \in \Omega$ at a time t is represented as $h_t(x, y)$. Here we describe a time t in the form of $t = YYYYMM$, where $YYYY$ and MM denote a year and month. For each month, *psiclone* calculates a unique COT representation, Reeb graph, and the partition plot from the SSH h_t, as shown in Fig. 3b. The COT representations contain an a_2 symbol attached to the Shikoku Island throughout the whole analysis period, and the COT symbols on the left side of the a_2 symbol indicate topological features on the northern side of the Kuroshio and Kuroshio Extension. Hence, we utilize the region of influence represented by a_- on the left side of the a_2 symbol in the COT representations. The algorithm to detect the stable Kuroshio meanderings south of the Kanto and Tokai districts comprises four steps. First, we identify domains where cyclonic eddies stay over 3 months by focusing on the region of influence associated with the COT symbols a_-. Second, we create chronological links between at present and previous months by tracking the geometric centers of the cyclonic eddies. Third, we extract links expressing a stable cyclonic eddy entrapped by the Kuroshio current south of the Kanto and Tokai districts. Finally, we distinguish the detected meandering periods into the oNLM and LM. The details are described as follows:

At first, to identify domains with stable cyclonic eddies, we construct the union of the regions of influence enclosed by the saddle separatrices of the a_- streamline patterns, denoted by $A(h_t)$, at a time t, and then define the following histogram $C_{t,\Delta t}(\boldsymbol{x})$ estimating how long the region of influence stays over $\boldsymbol{x} \in \Omega$ in the time window of $[t - \Delta t/2, t + \Delta t/2)$:

$$C_{t,\Delta t}(\boldsymbol{x}) := \#\left\{ \tau \in \boldsymbol{N} \,\middle|\, t - \frac{\Delta t}{2} \le \tau < t + \frac{\Delta t}{2}, \boldsymbol{x} \in A(h_\tau) \right\} \tag{2}$$

where $\#A$ denotes the number of elements contained in a set A, τ denotes a month. In this study, we use $\Delta t = 6$ *months* to identify stable Kuroshio meanderings. The histogram $C_{t,\Delta t}(\boldsymbol{x})$ is calculated by adding 1 month whenever a region of influence in $A(h_\tau)$ exists over $\boldsymbol{x}$ in the period $\tau \in [t - \Delta t/2, t + \Delta t/2)$,and, therefore, $0 \le C_{t,\Delta t}(\boldsymbol{x}) \le \Delta t$. Figure 4a shows the histogram $C_{t,\Delta t}(\boldsymbol{x})$ constructed from the SSH in March 2005 ($t = 200503$). The *support* of the histogram with positive values consists of four connected domains (Fig. 4a): southwest of the Kyushu Island, between the Kyushu and Shikoku Islands, south of the Tokai district, and on the northern side of Kuroshio Extension. Since $C_{t,\Delta t}(\boldsymbol{x})$ means how long a cyclonic eddy represented by the a_- symbol stays within 3 months before and after at a time t, the high $C_{t,\Delta t}(\boldsymbol{x})$ values off the southern coast of the Tokai district are consistent with the LM. Consequently, we extract the disjoint domains B_t^n, where $C_{t,\Delta t}(\boldsymbol{x})$ is longer than the threshold $\theta := \Delta t/2 = 3$ *months* at a time t. We thus obtain the *union* of such disjoint domains $\mathfrak{B}_t = \{B_t^n\}_{n=1}^{N_t} \subset \Omega$, where N_t denotes the number of connected components (Fig. 4b). The resulting support of $C_{t,\Delta t}(\boldsymbol{x})$ are then divided into several connected components, belonging to $\mathfrak{B}_t$, and a large connected component with $C_{t,\Delta t}(\boldsymbol{x}) = 6$ *months* is located south of the Tokai district (a blue rectangle in Fig. 4b). This represents that the Kuroshio meandering with a cyclonic eddy is maintained 3 months before and after March 2005 in this domain.

In the second step, we track all connected components in $\mathfrak{B} = \cup_t \mathfrak{B}_t$ in the temporal direction to extract the period when the Kuroshio meanders south of the Kanto and Tokai districts. Specifically, we adopt a *chronological link* among the connected components in $\mathfrak{B}$ as follows: When the geometric center of a disjoint domain $B_{t+1}^{n'} \subset \mathfrak{B}_t$ at a time $t + 1$

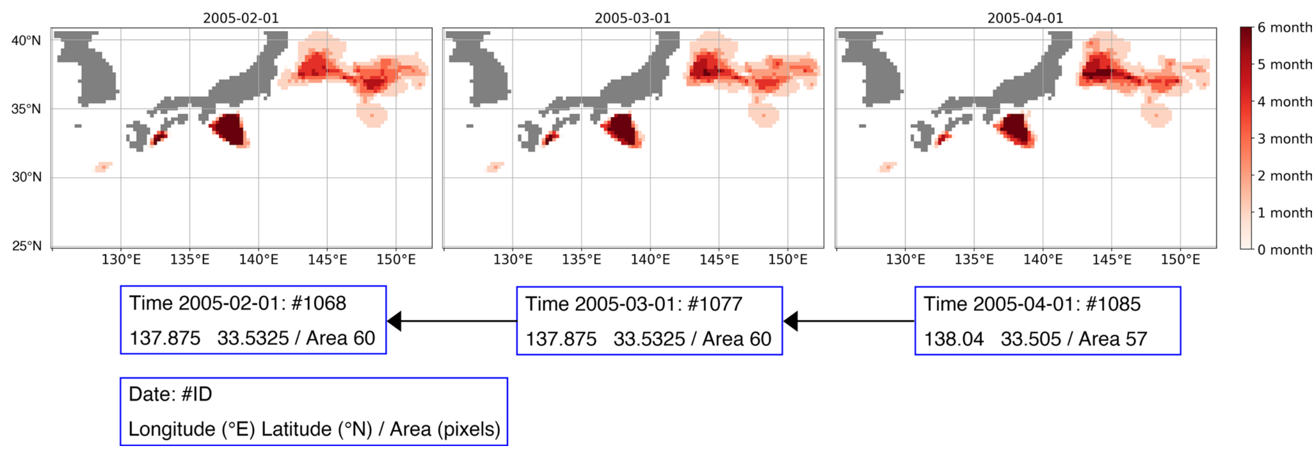

Fig. 5 As in Fig. 4b, but for February to April 2005 in the top panel and directed edges between the connected component inside the blue rectangle in B_t in the bottom panel. Each blue box contains a date and the ID number of connected component in the upper line, and the position of the geometric center and the number of pixels (i.e. area) of the domain in the lower line

is contained in a domain $B_t^n \subset \mathfrak{B}_t$ at a time t, we create a *directed edge* between them such as $B_{t+1}^{n'} \rightarrow B_t^n$, since the domain $B_{t+1}^{n'}$ is likely to move from the domain B_t^n. Here, the geometric center of a domain B_t^n is estimated from the position vectors for a certain fixed point in B_t^n. Applying this operation to all domains in $\mathfrak{B}$ leads to a *directed acyclic graph (DAG)* of $\mathfrak{B}$. The DAG of $\mathfrak{B}$ comprises several disjoint links, called *paths*, connecting the connected components in $\mathfrak{B}_t$ in the backward chronological order. The maximum number of nodes of DAG contained in a path is referred to as a *lifespan of the path*, expressing how many months the stable cyclonic eddy persists.

From February to April 2005, there are several connected components extracted in the first step as shown in Fig. 5. Here, we focus on a substantial connected component south of the Tokai district. Since the geometric center of the connected component in April 2005 is contained in that in March 2005, we create a directed edge linking between them. From March to February 2005, similarly, we can create a directed edge. All nodes in the link (bottom boxes in Fig. 5) contain the location of the geometric center and area of the connected component. We apply this procedure to all connected components during the whole analysis period. If the area of a disjoint domain at a time t is small, its geometric center is less likely to be contained in the previous month, and thus paths between the disjoint domains are hardly created.

In the third step, we identify paths associated with stable Kuroshio meanderings. Since a cyclonic eddy is located south of the Tokai and Kanto districts during the LM and oNLM periods (Fig. 1a), respectively, we pick up paths of the disjoint domains whose geometric centers exist within [133°– 141°E, 31°– 35°N]. We then extract nodes and connecting directed edges from the obtained paths if the area exceeds $S_0 (= 40\,pixels)$ and the lifespan exceeds three months to detect stable meanderings. The area of $S_0 = 40\,pixels$ roughly corresponds to an eddy with the 100 km radius. We have confirmed that only the number of nodes of DAG is slightly changed at $S_0 = 35 - 45\,pixels$.

Finally, we distinguish the obtained meandering periods into the oNLM and LM periods. As described in Sect. 1, the Kuroshio meanders southward off the Kanto district passing through the southern gate of the Izu Ridge during the oNLM period, whereas it forms southward meandering off the Tokai district and then flows along the southern coast around the Kanto district during the LM period. Consequently, we define the oNLM (LM) events if the Kuroshio flows south (north) of 34°N along 140°E section. Here, the Kuroshio position is defined as the southernmost latitude of the COT symbol $a\_$ representing a cyclonic eddy. If any cyclonic eddies do not exist south of the Kanto district along 140°E, the Kuroshio position is assumed to be 35.5°N.

4 Results

We apply the TFDA algorithm to the SSH dataset from the AVISO to detect the Kuroshio meanderings from April 1993 to January 2020. We note that the results are obtained during this period because of the analysis window of ± 3 months although we use the AVISO dataset from January 1993 to April 2020. To check the accuracy of the temporal variations in the Kuroshio position extracted by TFDA, we first compare the Kuroshio southernmost latitude south of the Tokai district (136°–140°E) detected by the JMA and TFDA (Fig. 1b). Here, we define the southernmost latitude of the Kuroshio as that of the COT symbol $a\_$ within 136°–140°E.

As clear from Fig. 1b, the temporal variations in the Kuroshio position detected by the JMA and TFDA correspond well with each other, and a correlation coefficient is 0.997. However, the Kuroshio position by TFDA is located north of the JMA throughout the whole period, and the bias relative to the JMA is 0.90°. This is probably because the TFDA captures the northern edge of the Kuroshio current because of the definition that the Kuroshio position is detected by the southernmost latitude of the cyclonic eddy (figure not shown). From the above results, it is concluded that TFDA well captures the temporal variations in the Kuroshio position, although the Kuroshio position by TFDA shows the northward shifted bias.

4.1 Kuroshio meandering episodes

Figures 1b, c, 6, and 7 show the following five episodes with the Kuroshio meanderings identified by the TFDA algorithm: episode A from September 2004 to June 2005; episode B from October 2013 to February 2014; episode C from September to December 2016; episode D from October 2017 to March 2019; and episode E from September 2019 to January 2020. As clear from the definition in subsection 3.3, this study extracts the meanderings that persist longer than three months and whose area in the cyclonic eddy associated with the meanderings exceeds 40 pixels (Figs. 6 and 7b). The JMA reports that the Kuroshio LM occurs at two times in the analysis period based on the southernmost latitude position in 136°–140°E and the sea level difference between Kushimoto and Uragami (Fig. 1b, c): from July 2004 to August 2005 and after August 2017 (ongoing in April 2022).
During the episodes A, D, and E, the Kuroshio flows south of 33°N off the Tokai district (Fig. 1b), and then north of 35°N off the Kanto district (Fig. 7a). Furthermore, these episodes are almost consistent with the two LM periods detected by the JMA. In April–August 2019 between episodes D and E, however, the area of the cyclonic eddy is smaller than 40 pixels (Fig. 7b) and, therefore, the TFDA algorithm does not detect meanderings. Its details will be discussed in subsection 4.2.

During the episodes B and C, as shown in Figs. 1b and 7a, the Kuroshio tends to flow north of 33°N off the Tokai district and then south of 34°N off the Kanto district. Figure 8 shows the partition plots and nodes of Reeb graphs on the left, and the regions of influence only shading the COT symbol a_{-} on the right panels around the episode B period (from August 2013 to March 2014). The COT representation for each month is also shown at the top of the panels. In August 2013 (i.e., two months before the episode B starts), the southward meandering with the COT symbol a_{-}^{2} is located south of the Tokai district, moving eastward to off the southern coast of the Kanto district in September 2013. This is consistent with the announcement of the Kuroshio southward meandering south of the Tokai district in August 2013 on the JMA Web site (https://www.data.jma.go.jp/gmd/kaiyou/shindan/rinji/2013/03/kuroshio_stream201308.html). From October 2013 to February 2014, the meandering stays at almost the same position with the increase of the cyclonic eddy area. Although the period of the episode C is the shortest among the five episodes, it is shown that the Kuroshio meandering located south of the Tokai district in September 2016 moves to south of the Kanto district in October 2016, and then the Kuroshio passes around the southern gate of the Izu Ridge off the southern coast of the Kanto district in October–December 2016 as is similar to the episode B (figure not shown). Therefore, the episodes B and C are concluded to be the oNLM period.

Although Fig. 2a of Sugimoto and Hanawa (2012) shows that the oNLM occurs more frequently than this study, this discrepancy is caused by the definition of the event in the TFDA algorithm. In this study, we extract the stable Kuroshio meandering events with the period longer than three months and the area of the cyclonic eddy larger than 40 pixels. However, we might be able to identify more meandering events if the area of the cyclonic eddy in the TFDA algorithm is set to 20 pixels (Fig. 7b). Precise validation of the threshold is out of the scope of this study.

4.2 Topological features during the meandering periods

In this subsection, we focus on the topological features near the termination of the meandering periods. In January 2014 (i.e., 1 month before the end of the episode B in Fig. 8), for example, the TFDA algorithm indicates remarkable topological structure of $a_{-}^{3}(b_{--})$ inside of the cyclonic eddy; inner structure of the eddy a_{-}^{3} is topologically divided into subdomains with two elliptic centers enclosed by saddle separatrices of b_{--}. Before and after January 2014, a single elliptic center exists inside the eddy associated with the meandering. A similar topological structure can be detected near the end of episodes A and D (in May 2005 and April 2019 in Fig. 9, respectively) except for the episode C. Usui et al. (2011) also indicate the eddy break-up occurs at the decaying phase in an LM event in 2004/05. In May 2019 the cyclonic eddy is completely separated into two eddies as clear from a_{-}^{3} and a_{-}^{4} in the COT representation (Fig. 9), and the TFDA algorithm creates the link of $a_{-}^{3}(b_{--})$ in April 2019 only with

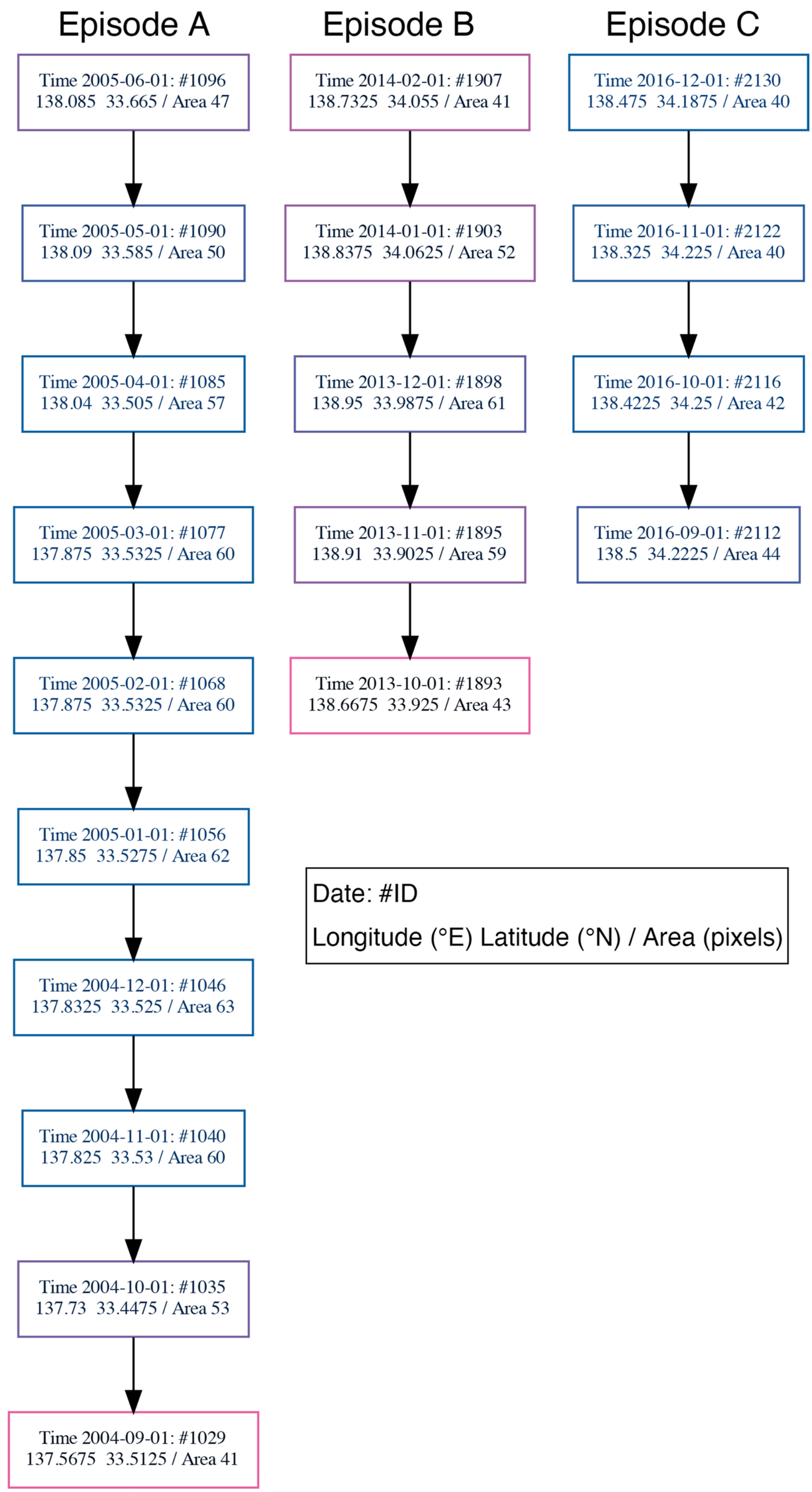

Fig. 6 List of meandering episodes identified by the TFDA algorithm. Arrows indicate the directed edges as in the bottom panel in Fig. 5. Each link corresponds to an episode that the meanderings persist from the date at the bottom to the top: episode A from September 2004 to June 2005; episode B from October 2013 to February 2014; episode C from September to December 2016; episode D from October 2017 to March 2019; and episode E from September 2019 to January 2020

Fig. 6 (continued)

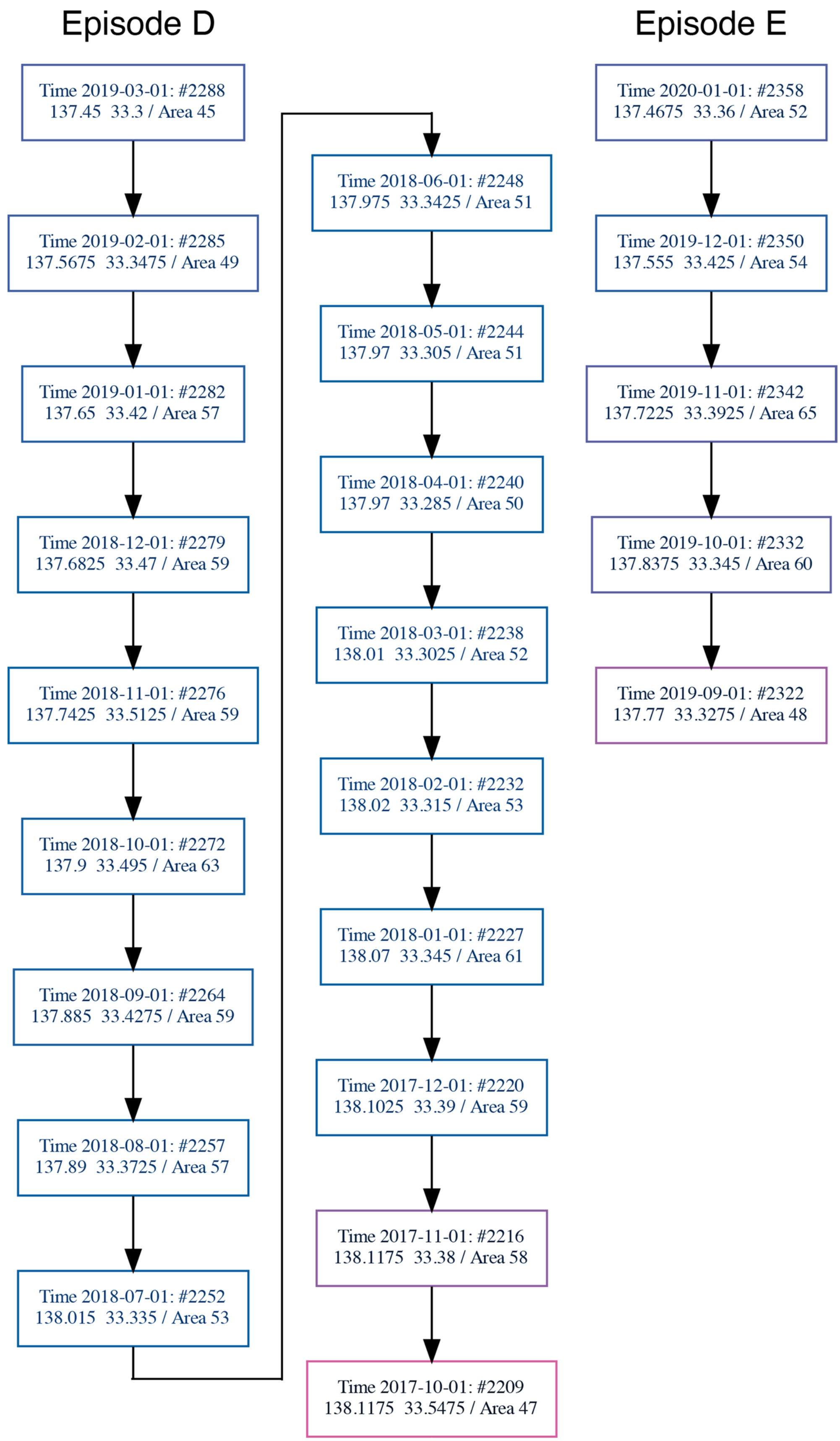

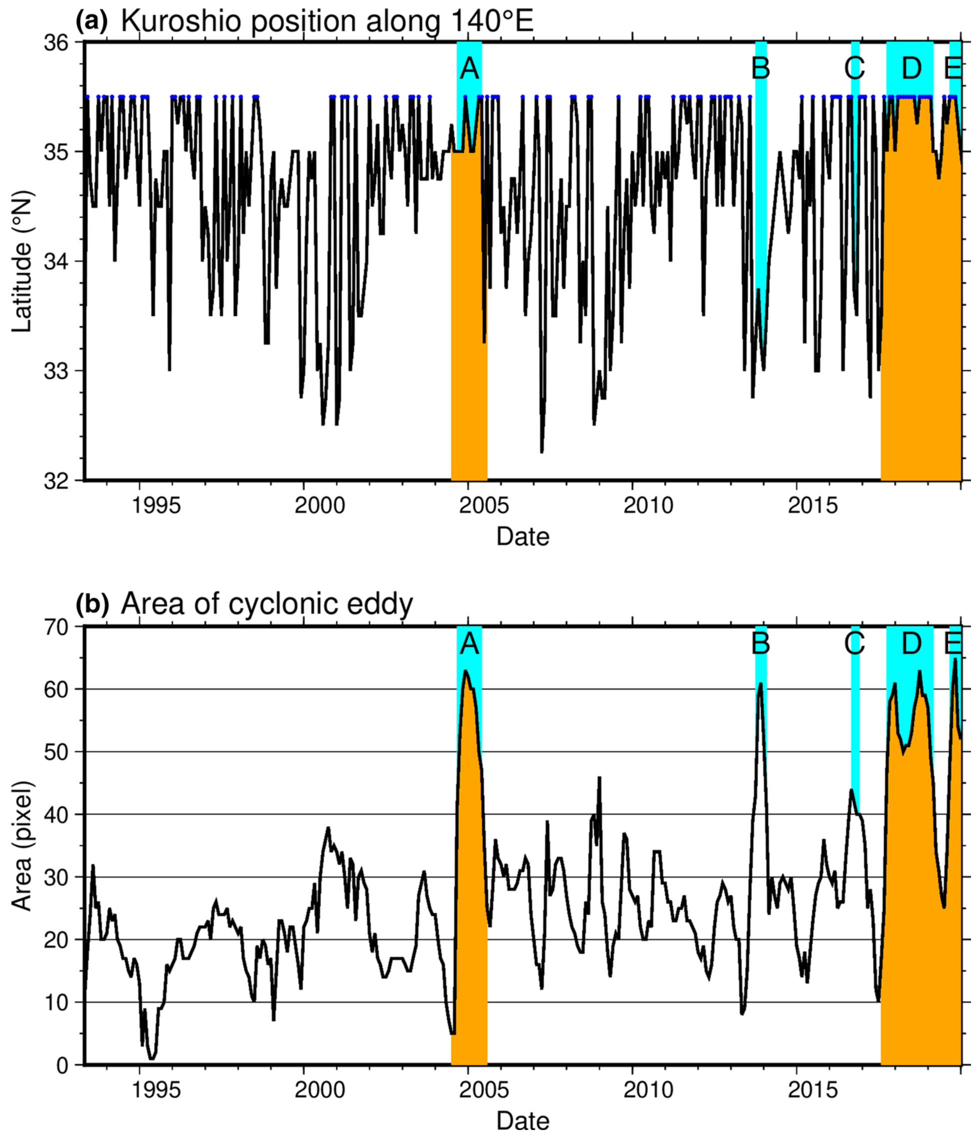

Fig. 7 **a** Kuroshio position off the Kanto district defined by the southernmost latitude of the COT symbol $a_{\_}$ along 140°E, and **b** area of the cyclonic with paths of the disjoint domains whose geometric centers exist within [133°–141°E, 31°–35°N]. In **a**, we assume that the Kuroshio is located at 35.5°N during no $a_{\_}$ symbols along 140°E (blue dots). In **a** and **b**, cyan (orange) shade indicates the meandering (LM) periods identified by the TFDA algorithm (JMA), and capital letters A–E denote the meandering episodes detected by the TFDA algorithm

the northern eddy $a_{\_}^{3}$ in May–June 2019. After July 2019 a single cyclonic eddy $a_{\_}^{3}$ starts to grow, and then the area of the eddy exceeds 40 pixels in September 2019. Thus, the TFDA algorithm appears to be difficult to identify the Kuroshio meandering events when the cyclonic eddy inside the meandering is unstable or separated into two eddies. However, this might provide beneficial information on whether the Kuroshio meandering is stable or unstable by comparing the results from the JMA.

When the topological structure of $a_{\_}^{3}(b_{\_\_})$ is detected inside of the cyclonic eddy, the temporal tendency of the Kuroshio transport across the 137°E section is positive (Fig. 10), and this might be related to the break-up of the cyclonic eddies and the meandering termination. This might be in agreement with results from sensitivity experiments conducted by Usui et al. (2013) that strong Kuroshio transport is not a favorable condition to maintain the Kuroshio LM for a long time. Therefore, as shown in a schematic illustration in Fig. 11, we can suggest a process how the Kuroshio meandering develops and terminates from the viewpoint of topology; After the size of single entrapped cyclonic eddy increases, the inner structure of this eddy is divided into two smaller cyclonic eddies near the termination phase, and finally the meandering structure is lost. This process corresponds to a transition between topological streamline patterns of structurally stable Hamiltonian vector fields through a structurally unstable Hamiltonian vector fields described in Sakajo and Yokoyama (2015).

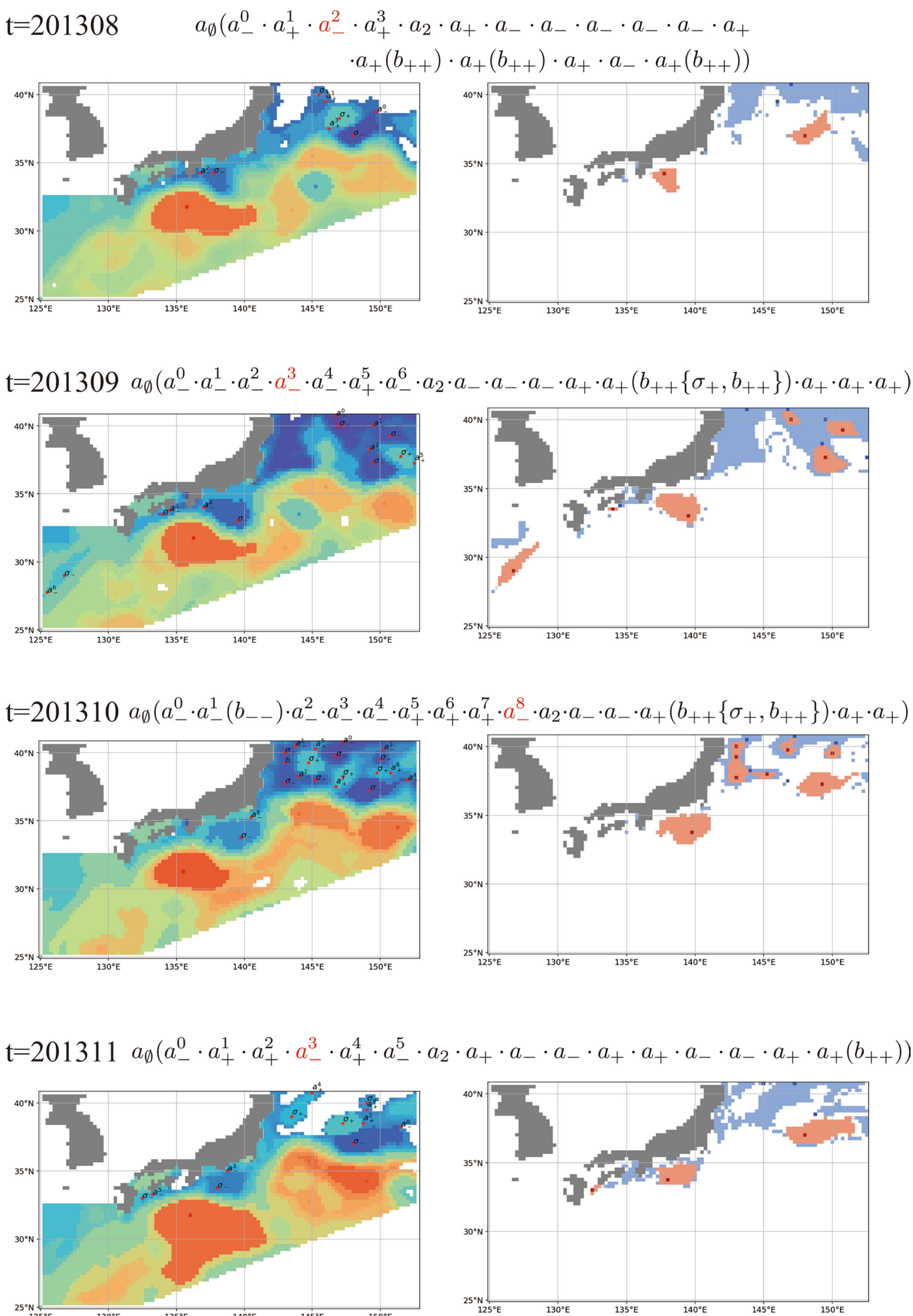

Fig. 8 The partition plots and corresponding nodes of Reeb graphs (left) and the regions of influence associated with a_- symbols (right) from August 2013 to March 2014 around the episode B (from October 2013 to February 2014). A string at the top of each figure denotes the COT representation. In the COT representation, red characters indicate the COT symbols associated with the meanderings. In the right panel, the red (blue) domains indicate the region of influence associated with a_- (a_+) on the left side of the COT symbol a_2

t=201312 $a_\emptyset(a_-^0 \cdot a_+^1 \cdot a_-^2 \cdot a_+^3 \cdot a_-^4 \cdot a_2 \cdot a_- \cdot a_- \cdot a_- \cdot a_+ \cdot a_- \cdot a_+ \cdot a_+(b_{++}) \cdot a_+)$

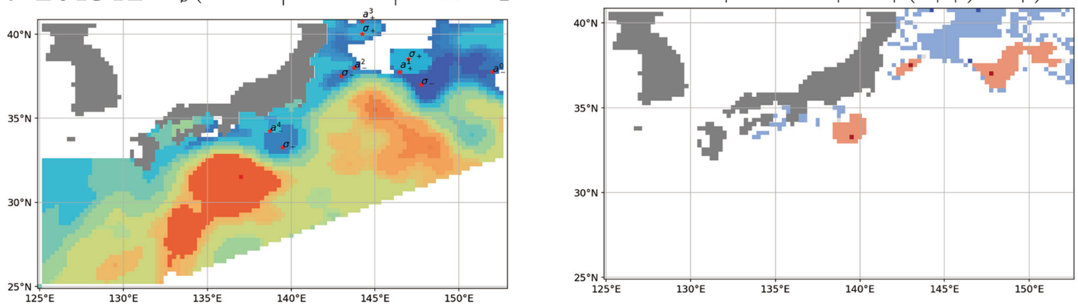

t=201401 $a_\emptyset(a_-^0 \cdot a_-^1 \cdot a_+^2 \cdot a_-^3(b_{--}) \cdot a_+^4 \cdot a_2 \cdot a_- \cdot a_+ \cdot a_- \cdot a_- \cdot a_+(b_{++}\{\sigma_+, b_{++}\{\sigma_+, b_{++}\}\}) \cdot a_+)$

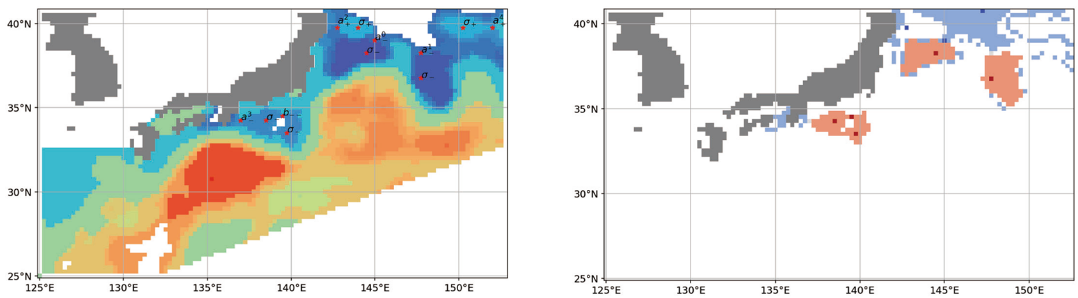

t=201402 $a_\emptyset(a_-^0 \cdot a_-^1 \cdot a_-^2 \cdot a_+^3 \cdot a_+^4 \cdot a_+^5 \cdot a_-^6 \cdot a_-^7 \cdot a_2 \cdot a_- \cdot a_-$
$\cdot a_+(b_{++}\{b_{++}, b_{+-}(b_{++}\{b_{++}, b_{++}\}, \sigma_-)\}) \cdot a_+)$

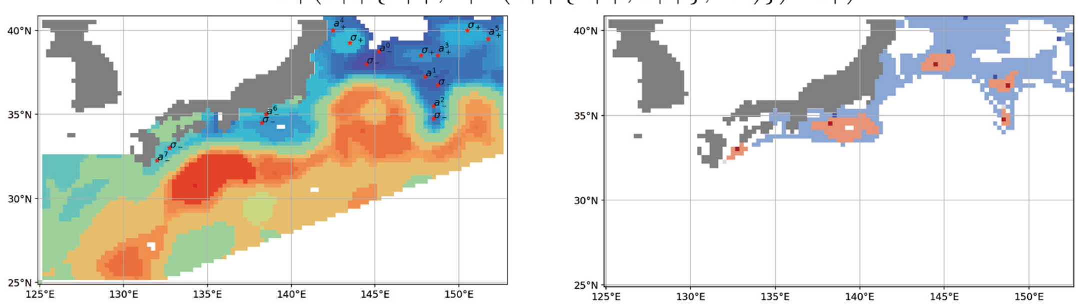

t=201403 $a_\emptyset(a_-^0(b_{--}) \cdot a_+^1 \cdot a_-^2 \cdot a_-^3 \cdot a_+^4 \cdot a_-^5 \cdot a_2 \cdot a_- \cdot a_- \cdot a_- \cdot a_-$
$\cdot a_+(b_{+-}(b_{++}\{\sigma_+, b_{+-}(b_{++}, \sigma_-)\}, \sigma_-)) \cdot a_+ \cdot a_+)$

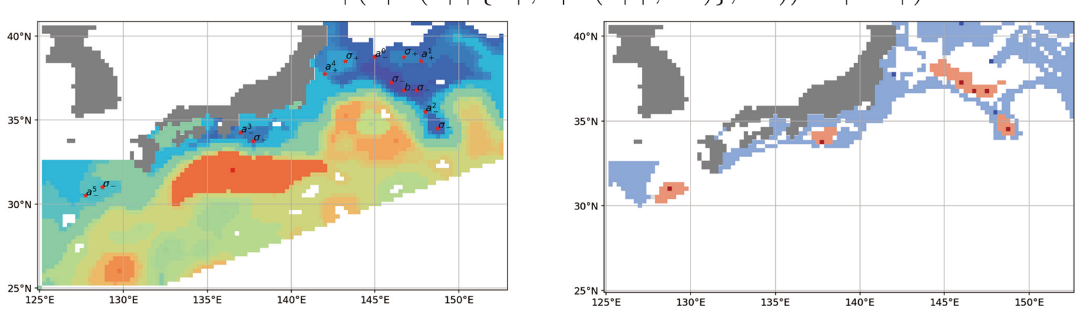

Fig. 8 (continued)

Fig. 9 As in Fig. 8, but for **a** from May to June 2005 in the episode A (from September 2004 to June 2005) and **b** from April to July 2019 just after the episode D (from October 2017 to March 2019)

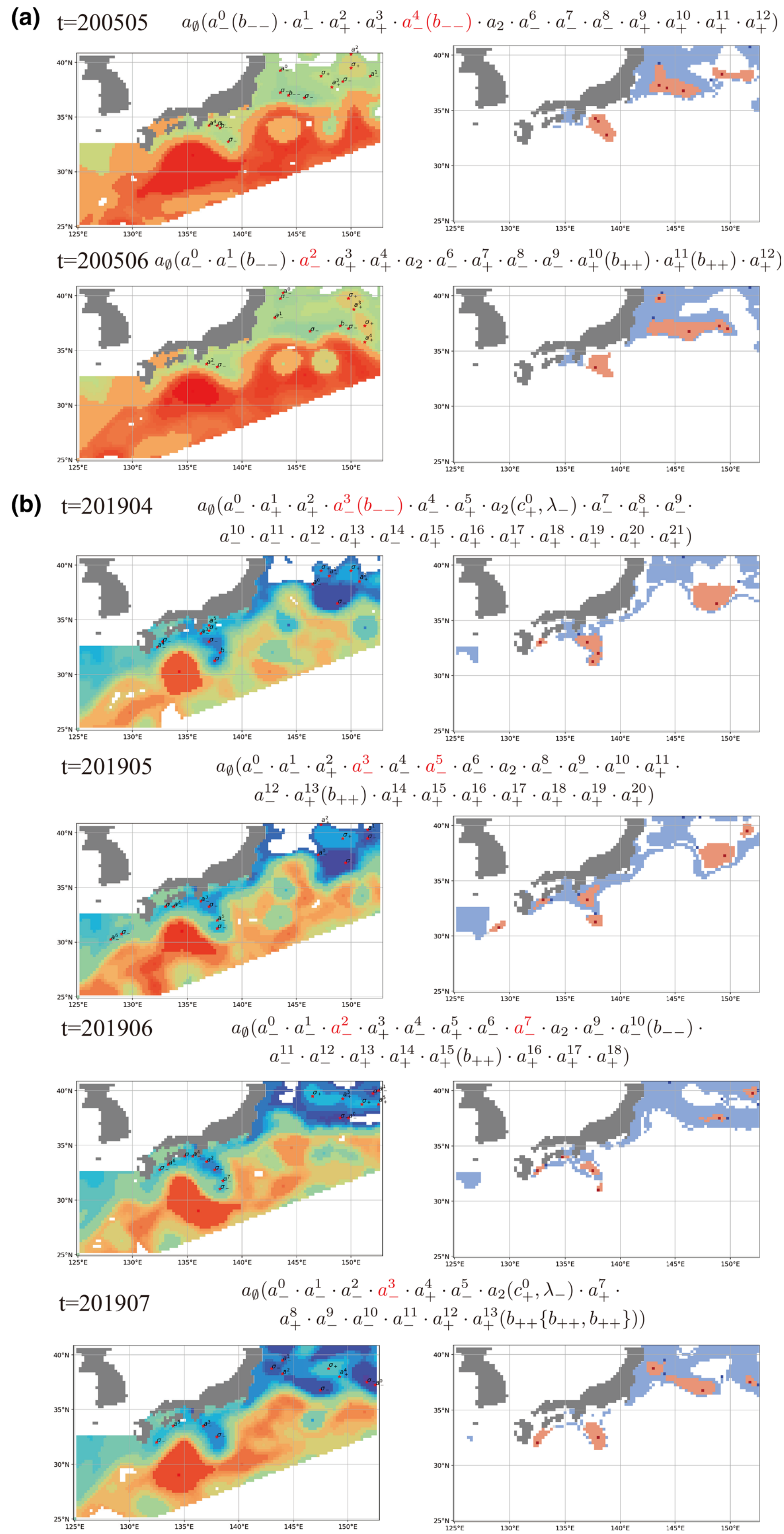

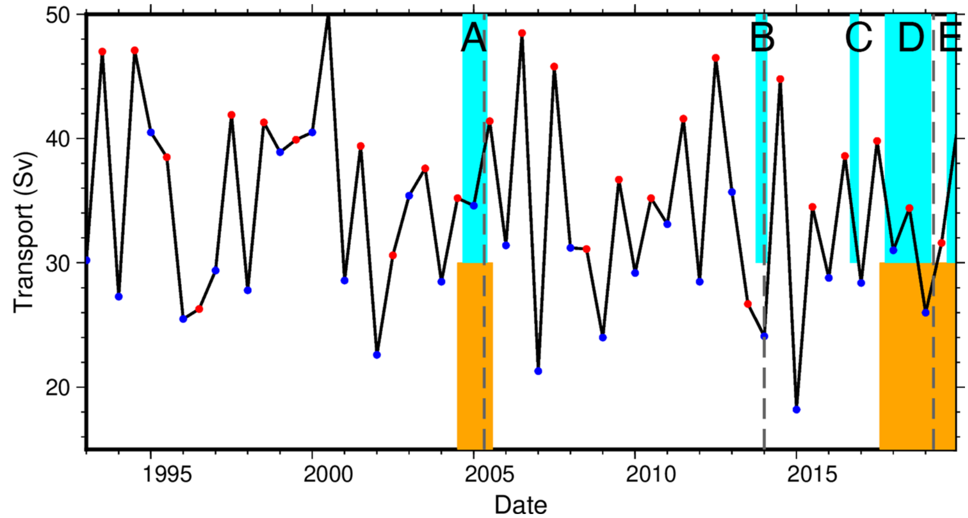

Fig. 10 Kuroshio transport across 137°E in boreal summer (red) and winter (blue). Gray dashed lines denote when the COT symbols $b\_\_$ are detected inside of the cyclonic eddy associated with the meanderings. Cyan (Orange) shade indicates the meandering (LM) periods detected by the TFDA algorithm (JMA). Capital letters A–E show the meandering episodes detected by the TFDA algorithm

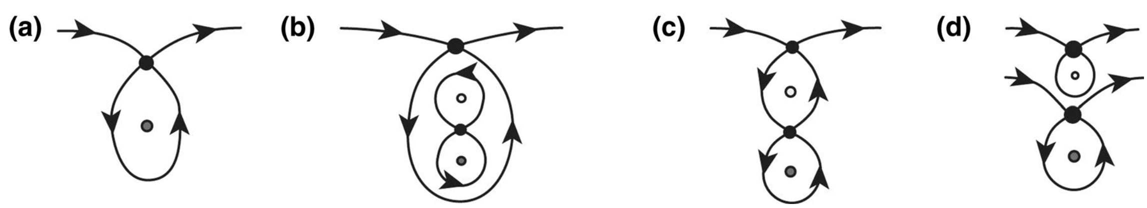

Fig. 11 Schematic diagram of a topological change in the inner core of the cyclonic eddy entrapped by the Kuroshio meanderings

5 Conclusion

The TFDA algorithm is developed and applied to the SSH gridded dataset to identify the Kuroshio meanderings from April 1993 to January 2020. The algorithm detects the stable Kuroshio oNLM and LM periods when the meandering with a cyclonic eddy, whose radius is larger than about 100 km, persists longer than three months. It also extracts the time series of the Kuroshio southernmost latitude in 136°–140°E south of the Tokai district and along 140°E south of the Kanto district, respectively, to confirm the accuracy of its temporal variation and distinguish the oNLM and LM periods. The temporal variation of the Kuroshio southernmost position south of the Tokai district detected by the TFDA corresponds well to that by the JMA (Fig. 1b), but it is located north of that by the JMA throughout the entire analysis period. This is because the TFDA algorithm detects the northern edge of the Kuroshio whereas the JMA captures the center of the Kuroshio.

We detect the following five meandering periods (Figs. 1b, c, 6, and 7): episode A from September 2004 to June 2005; episode B from October 2013 to February 2014; episode C from September to December 2016; episode D from October 2017 to March 2019; and episode E from September 2019 to January 2020. During the episodes A, D, and E, the Kuroshio largely meanders southward off the Tokai district (Fig. 1b) and flows along the southern coast of the Kanto district (Fig. 7a). Furthermore, these episodes are almost consistent with the occurrence period of the Kuroshio LM reported by the JMA. Therefore, the episodes A, D, and E are concluded to be the LM periods. During the episodes B and C, the Kuroshio is located near the southern coast of the Tokai district (Figs. 1b, 8) and then meanders southward off the Kanto district (Figs. 7a, 8). Consequently, the episodes B and C are assigned to the oNLM period. Thus, the TFDA algorithm can identify the difference between stable LM and oNLM path.

In addition, the topological features obtained by TFDA suggest a process of how the meandering develops and terminates. With the increase of the size of a single cyclonic eddy and the positive temporal tendency of the Kuroshio transport, the cyclonic eddy is divided into two small eddies near the termination period, and finally the meandering structure is lost (Figs. 8–11). Usui et al. (2011) also indicates the break-up of the cyclonic eddy at the decaying phase of the LM event in 2004-05. This study first demonstrates topologically the break-up of a single large eddy entrapped by the Kuroshio into two small eddies near the termination phase of the most meandering events. Although it is interesting to investigate the physical mechanisms of the meandering formation and termination as in the previous studies (e.g. Tsujino et al. 2006; Usui et al. 2011), this is beyond the scope of the present work. We will report the results of ensemble sensitivity analyses using an ensemble Kalman filter-based regional ocean data assimilation and prediction system (Ohishi et al. in review) in a future study.

This study has applied TFDA to the oceanography field at the first time as far as we know. Although this study uses the monthly-mean SSH to identify the stable Kuroshio meandering south of Japan because of the computational cost and visualization, we are now improving *psiclone* to reduce the computation cost. The TFDA algorithm would become more useful tool to provide instantaneous flow features and presages of the termination of the Kuroshio meandering period. This can be carried out by applying to near-real-time daily observational datasets and outputs from ocean data assimilation and prediction systems. Also, it further could be developed for an eddy tracking method based on the topological features obtained by TFDA. Such directions are under way.

Acknowledgements TU is supported by JST ACT-X (#JPMJAX1906). TS is partially supported by JST MIRAI (#JPMJMI18G3, #JPMJMI22G1), the RIKEN iTHEMS program. SO is supported by JST AIP Grant Number JPMJCR19U2, Japan; MEXT (#JPMXP1020200305) as "Program for Promoting Researches on the Supercomputer Fugaku" (Large Ensemble Atmospheric and Environmental Prediction for Disaster Prevention and Mitigation); the COE research grant in computational science from Hyogo Prefecture and Kobe City through Foundation for Computational Science; JST, SICORP Grant Number JPMJSC1804, Japan; JSPS KAKENHI Grant Number JP19H05605; the JAXA; JST, CREST Grant Number JPMJCR20F2, Japan; Cabinet Office, Government of Japan, Cross-ministerial Moonshot Agriculture, Forestry and Fisheries Research and Development Program, “Technologies for Smart Bio-industry and Agriculture”(funding agency: Bio-oriented Technology Research Advancement Institution) No. JPJ009237; RIKEN Pioneering Project "Prediction for Science"; RIKEN Engineering Network Project.

Funding JST-Mirai Program, JPMJMI18G3, Takashi Sakajo, JPMJMI22G1, Takashi Sakajo, JST ACT-X, JPMJAX1906, Tomoki Uda, AIP Network Laboratory, JPMJCR19U2, Shun Ohishi.

References

Ambe D, Imakawi S, Uchida H, Ichikawa K (2004) Estimating the Kuroshio axis south of Japan using combination of satellite altimetry and drifting buoys. J Oceanogr 60:375–382. https://doi.org/10.1023/B:JOCE.0000038343.31468.fe

Aoki K, Miyazawa Y, Hihara T, Miyama T (2020) An objective method for probabilistic forecasting of multimodal kuroshio states using ensemble simulation and machine learning. J Phys Oceanogr 50:3189–3204. https://doi.org/10.1175/JPO-D-19-0316.1

Ducet N, Le Traon PY, Reverdin G (2000) Global high-resolution mapping of ocean circulation from TOPEX/Poseidon and ERS-1 and -2. J Geophys Res 105:19477–19498. https://doi.org/10.1029/2000JC900063

Hirose N, Usui N, Sakamoto K et al (2019) Development of a new operational system for monitoring and forecasting coastal and open-ocean states around Japan. Ocean Dyn 69:1333–1357. https://doi.org/10.1007/s10236-019-01306-x

Kawabe M (1980) Sea level variations along the south coast of Japan and the large meander in the Kuroshio. J Oceanogr Soc Japan 36:97–104. https://doi.org/10.1007/BF02312095

Kawabe M (1995) Variations of current path, velocity, and volume transport of the kuroshio in relation with the large meander. J Phys Oceanogr 25:3103–3117. https://doi.org/10.1175/1520-0485(1995)025%3c3103:VOCPVA%3e2.0.CO;2

Maximenko N, Niiler P, Rio MH et al (2009) Mean dynamic topography of the ocean derived from satellite and drifting buoy data using three different techniques. J Atmos Ocean Technol 26:1910–1919. https://doi.org/10.1175/2009JTECHO672.1

Miyazawa Y, Yamane S, Guo X, Yamagata T (2005) Ensemble forecast of the Kuroshio meandering. J Geophys Res C Ocean 110:1–14. https://doi.org/10.1029/2004JC002426

Miyazawa Y, Zhang R, Guo X et al (2009) Water mass variability in the western North Pacific detected in a 15-year eddy resolving ocean reanalysis. J Oceanogr 65:737–756. https://doi.org/10.1007/s10872-009-0063-3

Nakamura H, Nishina A, Minobe S (2012) Response of storm tracks to bimodal kuroshio path states south of Japan. J Clim 25:7772–7779. https://doi.org/10.1175/JCLI-D-12-00326.1

Nakata H, Funakoshi S, Nakamura M (2000) Alternating dominance of postlarval sardine and anchovy caught by coastal fishery in relation to the Kuroshio meander in the Enshu-nada Sea. Fish Oceanogr 9:248–258. https://doi.org/10.1046/j.1365-2419.2000.00140.x

Ohishi, S., Hihara, T., Aiki, H., Ishizaka, J., Miyazawa, Y., Kachi, M., and Miyoshi, T.: An ensemble Kalman filter system with the Stony Brook Parallel Ocean Model v1.0, Geosci. Model Dev. Discuss. [preprint], https://doi.org/10.5194/gmd-2022-40, in review, 2022.

Ohishi, S., Miyoshi, T., and Kachi, M.: An EnKF-based ocean data assimilation system improved by adaptive observation error inflation (AOEI), Geosci. Model Dev. Discuss. [preprint], https://doi.org/10.5194/gmd-2022-91, in review, 2022.

Sakajo T, Yokoyama T (2015) Transitions between streamline topologies of structurally stable Hamiltonian flows in multiply connected domains. Phys D Nonlinear Phenom 307:22–41. https://doi.org/10.1016/j.physd.2015.05.013

Sakajo T, Yokoyama T (2018) Tree representations of streamline topologies of structurally stable 2D incompressible flows. IMA J Appl Math 83:380–411. https://doi.org/10.1093/imamat/hxy005

Sugimoto S, Hanawa K (2012) Relationship between the path of the Kuroshio in the south of Japan and the path of the Kuroshio Extension in the east. J Oceanogr 68:219–225. https://doi.org/10.1007/s10872-011-0089-1

Sugimoto S, Qiu B, Kojima A (2020) Marked coastal warming off Tokai attributable to Kuroshio large meander. J Oceanogr 76:141–154. https://doi.org/10.1007/s10872-019-00531-8

Taburet G, Sanchez-Roman A, Ballarotta M et al (2019) DUACS DT-2018: 25 years of reprocessed sea level altimeter products. Ocean Sci 2014:1–30. https://doi.org/10.5194/os-15-120

Tsujino H, Usui N, Nakano H (2006) Dynamics of Kuroshio path variations in a high-resolution general circulation model. J Geophys Res 111:C11001. https://doi.org/10.1029/2005JC003118

Uda T, Sakajo T, Inatsu M, Koga K (2021) Identification of atmospheric blocking with morphological type by topological flow data analysis. J Meteorol Soc Japan 99:1169–1183. https://doi.org/10.2151/jmsj.2021-057

Uda T, Yokoyama T, Sakajo T (2019) Algorithms converting streamline topologies for 2D Hamiltonian vector fields using Reeb graphs and persistent homology. Trans Japan Soc Ind Appl Math 29:187–224. https://doi.org/10.11540/jsiamt.29.2 187

Usui N, Tsujino H, Fujii Y, Kamachi M (2006) Short-range prediction experiments of the Kuroshio path variabilities south of Japan. Ocean Dyn 56:607–623. https://doi.org/10.1007/s10236-006-0084-z

Usui N, Tsujino H, Nakano H et al (2011) Decay mechanism of the 2004/05 Kuroshio large meander. J Geophys Res 116:C10010. https://doi.org/10.1029/2011JC007009

Usui N, Tsujino H, Nakano H, Matsumoto S (2013) Long-term variability of the Kuroshio path south of Japan. J Oceanogr 69:647–670. https://doi.org/10.1007/s10872-013-0197-1

Yokoyama T, Sakajo T (2013) Word representation of streamline topologies for structurally stable vortex flows in multiply connected domains. Proc R Soc A Math Phys Eng Sci 469:20120558. https://doi.org/10.1098/rspa.2012.0558